ELSEVIER

Journal of Fluids and Structures 23 (2007) 1119–1136

JOURNAL OF FLUIDS AND STRUCTURES

www.elsevier.com/locate/jfs

Spacing effects on hydrodynamics of heave plates on offshore structures

L. Tao[a,*], B. Molin[b], Y.-M. Scolan[b], K. Thiagarajan[c]

[a]*School of Engineering, Griffith University, PMB50 GCMC, Qld 9726, Australia*
[b]*Laboratoire d'Hydrodynamique, Ecole Generaliste d'Ingenieurs de Marseille, 13 451 Marseille cedex 20, France*
[c]*School of Oil and Gas Engineering, The University of Western Australia, 35 Stirling Hwy, Crawley, WA 6009, Australia*

Received 24 February 2006; accepted 31 March 2007
Available online 18 June 2007

Abstract

The nonlinear viscous flow problem associated with a heaving vertical cylinder with two heave plates in the form of two circular disks attached is solved using a finite difference method. Numerical experiments are carried out to investigate the spanwise length effects on the hydrodynamic properties, such as added mass and damping coefficients. Over a Keulegan–Carpenter (KC) number range from 0.1 to 0.6 at frequency parameter ($\beta = 7.869 \times 10^7$), calculations indicate that a KC-dependent critical value of spanwise length L/D_d (L—the distance between the disks, and D_d—the diameter of the disks) exists. A significant influence of L/D_d on the vortex shedding patterns around the disks and the hydrodynamic coefficients is revealed when L/D_d is smaller than the critical value due to strong interaction between vortices of different disks. Beyond that limit, however, both added mass and damping coefficients are shown to be rather stable, indicating the independence of the vortex shedding processes of different disks.
© 2007 Elsevier Ltd. All rights reserved.

Keywords: Heave plate; Spar; Viscous damping; Added mass; Vortex shedding

1. Introduction

The spar platform has attracted much attention of researchers and design engineers in offshore engineering. It is one of the most reliable and cost effective structure for offshore oil and gas exploration in deep water. Due to reduced amplitudes of oscillations in the vertical plane (i.e. heave, pitch and roll), one of the principal advantages of the spar concept compared to other conventional floating systems is the use of dry well-heads and rigid risers. Typically a spar has a natural heave period above 25 s, which in most circumstances is sufficiently outside the prevailing wave frequency range. However, a spar may still suffer from resonant heave motions, which are excessive for riser integrity, in sea states with long peak periods due to its low damping. A typical example is in the swell waves offshore West Africa, with peak period lying in the 23–25 s range. Such a wave spectrum will have appreciable energy even at up to 30 s.

The heave response of a spar platform depends on the linear and nonlinear wave exciting forces, natural period of the system and hydrodynamic damping forces. The earliest spar concept, called the classic spar, with cylindrical shape and constant cross section obtained its low heave characteristics due to its deep draft resulting in low wave excitation force.

*Corresponding author. Fax: +61 7 55528065.
E-mail address: l.tao@griffith.edu.au (L. Tao).

0889-9746/$ - see front matter © 2007 Elsevier Ltd. All rights reserved.
doi:10.1016/j.jfluidstructs.2007.03.004

The heave natural period (T) of a classic spar structure is primarily dependent on its draft and inertia coefficient,

$$T = 2\pi\sqrt{\frac{T_d C_m}{g}}, \tag{1}$$

where T_d and C_m represent the draft of the spar and the inertia coefficient which equals to $1 + C_a$ with C_a being the added mass coefficient, g is the acceleration due to gravity, respectively. Eq. (1) indicates that the long heave natural period can be achieved by extending the draft of the spar column. However, increasing the draft, and consequently increasing the system mass, is normally subject to many other considerations in the design, such as the cost of construction, transport and installation of the structure.

In addition to increasing the heave natural period of a spar platform beyond the dominant wave energy range, increasing heave damping is another efficient means of reducing the heave response. Apart from the damping forces from the mooring system, a classic spar hull is considered a lightly damped system. Ways of increasing heave damping may thus offer significant advantages in terms of heave stabilisation of the spar.

Recent developments of the spar concept led to the second generation of truss spars. Based on the consideration of both added mass and damping characteristics, heave plates oriented normal to the spar axis are introduced in the truss structure. The plates increase added mass and damping when the spar moves in heave, which results in longer heave natural period (see Eq. (1)), as well as reduced motion due to higher damping.

Appendages have long been used to control amplitudes of undesirable motions of structures in fluids. Typical examples are bilge keels on ships and helical strakes which are widely applied to spar hulls. Srinivasan et al. (2005) presented a new concept of truss pontoons with heave plates on a semi-submersible which had reduced vertical plane motions. A similar idea without the truss structure was used by Cermelli and Roddier (2005) on a minimal platform. Further, the use of plates was generalised to other cylindrical structures. In particular several offshore buoys were found to have favourable motion characteristics with a base plate (also called skirt) structure [see e.g. Cozijn et al. (2005), for application to a CALM buoy].

Thiagarajan and Troesch (1998) measured the heave damping of a vertical cylinder with a disk attached to the base. Their experiments were conducted in the range of KC $= 0.1\sim1.0$ ($= 2\pi a/D_d$, a is the amplitude of heave oscillation; D_d is the diameter of the disk) and frequency parameter $\beta = 89\,236$ (β is defined as $D_d^2 f/v$, where f is frequency and v is kinematic viscosity). The results showed that the heave damping induced by the disk is linear with the amplitude of oscillation. The disk was found to increase the form drag coefficient (C_d) two-fold. However, previous investigations were primarily focused on the oscillation suppression due to the damping increased by the external devices.

Tao and Thiagarajan (2003a, b) investigated the hydrodynamics of a heaving vertical cylinder with a single disk attached at the keel. The effects of the geometry of the disk, such as aspect ratio t_d/D_d (t_d is the thickness of the disk) and diameter ratio D_d/D_c (D_c is the diameter of the cylinder or spar) on heave damping and added mass were examined. The aspect ratio of disk t_d/D_d was found to have the most striking effect on the vortex shedding and the viscous damping, especially when the aspect ratio is small. However, the effect of changing aspect ratio on damping was also found to be dependent strongly on KC number, while D_d/D_c was found to have a significant impact on the hydrodynamics, especially on added mass. The recommendation of a spar hull and disk geometry was made to achieve optimum heave response.

In order to obtain better heave characteristics of a spar, several heave plates attached to a spar hull or truss spar were proposed. Recent studies by Downie et al. (2000) and Magee et al. (2000) revealed that the increased added mass is the dominant contribution to the reduction of the heave amplitude of a classic spar with heave plates attached or a truss spar compared to the increase in damping resulting from the heave plates. However, damping is also important for relatively shallow draft spar or truss spar designs. A typical example is the truss spar proposed for West Africa, where very long swells, with periods approaching the heave natural period, occasionally occur. Preliminary study of Thiagarajan et al. (2002) has shown a classic spar will suffer heave resonance.

In their experimental study, Prislin et al. (1998) carried out model tests on an array of solid square plates, oscillating perpendicular to their plane in an otherwise quiescent fluid. Based on the measurements, Prislin et al. (1998) concluded that the added mass coefficient for the single plate does not depend on the Reynolds number higher than 10^5. However, this conclusion could not be extended to the case of multiple plates due to insufficient data on the variability in Reynolds number. It was further pointed out by the authors that special precautions should be taken when analysing model test results for a spar with heave plates. Because of a relatively low Reynolds number for the model in comparison to the full scale (the ratio is about two orders of magnitude), drag coefficient for the model plate can be two to three times larger than that for full scale spar. However, Thiagarajan and Troesch (1998) as well as Lake et al. (2000) have argued that the predominant damping contribution from plate edges arises from convective motion of vorticity and hence should be scalable to full scale.

Based on perfect fluid and irrotational flow assumptions, Molin (2001) studied arrays of porous disks in oscillatory flow perpendicular to their planes, similar to the configuration of a truss spar. The author considered the size of openings as the main variable to study effect of porosity on heave plate hydrodynamics. It was found that no extra damping can be gained by making the disk porous when KC is greater than 1. However, the heave damping can be increased by a factor 4 to 5 with porosity slightly below 20% in the case of a KC number around 0.2. Moreover, the added mass becomes zero when the KC number approaches zero indicating the sensitivity of the added mass coefficient with motion amplitude. Therefore, it is of great importance in the vertical resonance of a spar platform. However, in the potential flow approach of Molin (2001), the form damping due to the edges of the disks was not included, but instead was calculated explicitly using empirical methods.

The optimised spacing between the heave plates, which leads to maximum damping and added mass for a given geometry of the heave plate, is a critical issue in the hydrodynamic design of a deep-water structure such as a spar or truss spar. In this paper, viscous flow generated by a spar column with two solid disks of variable spacings attached is solved numerically. The vortex shedding flow patterns induced by the sharp edges of the disks are examined based on numerical flow visualisation. The associated hydrodynamic properties, i.e. added mass coefficient and damping ratio are calculated in the realistic parameter range of a prototype spar. The accurate values of the above hydrodynamic coefficients will provide solid basis for the further prediction of the effects of the heave plates on the spar responses.

2. Theoretical formulation

2.1. Governing equations

The flow generated by a vertical cylinder with two attached disks, oscillating along its axis can be idealised as axi-symmetric by neglecting three-dimensional effects at relatively small amplitudes (see Fig. 1). The governing equations for the time-dependent unsteady flow are the continuity and the Navier–Stokes equations for an incompressible viscous fluid. The nondimensional form of the governing equations in cylindrical polar coordinate system (r, y) are written as

$$\frac{1}{r}\frac{\partial(ru)}{\partial r}+\frac{\partial v}{\partial y}=0, \tag{2}$$

$$\frac{\partial u}{\partial t}+(\mathbf{V}\cdot\nabla)u=-\frac{\partial p}{\partial r}+\frac{1}{\mathrm{Re}'}\left(\nabla^2 u-\frac{u}{r^2}\right), \tag{3}$$

$$\frac{\partial v}{\partial t}+(\mathbf{V}\cdot\nabla)v=-\frac{\partial p}{\partial y}+\frac{1}{\mathrm{Re}'}(\nabla^2 v), \tag{4}$$

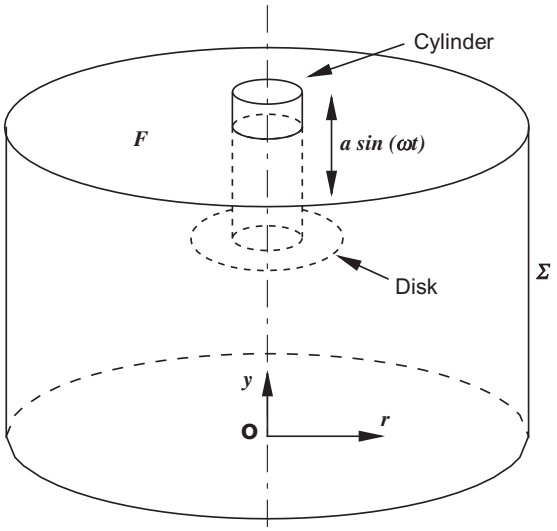

Fig. 1. Flow configuration for a cylinder with disks attached in heave.

where $\mathbf{V} = (u, v)$ is the velocity vector, (u, v) denote the radial and axial components of velocity, respectively, t the time, and p the dynamic pressure. In this paper, the governing equations and all physical quantities are presented in a nondimensional form. $\mathrm{Re}' = (R\sqrt{Rg})/v$ in Eqs. (3) and (4) arises due to the fundamental variables used in nondimensionalisation, i.e. density of fluid ϱ, acceleration of gravity g, and radius of the cylinder R.

In order to decouple the velocity and pressure field in the governing equations (3) and (4) and solve them alternately, the Poisson equation for pressure is derived by taking divergence of the momentum Eqs. (3) and (4). This gives

$$\nabla^2 p = -\frac{\partial \tilde{D}}{\partial t} - \left[\left(\frac{\partial u}{\partial r}\right)^2 + \left(\frac{\partial v}{\partial y}\right)^2 + 2\frac{\partial v}{\partial r}\frac{\partial u}{\partial y}\right] - \frac{u^2}{r^2}, \tag{5}$$

where $\tilde{D}$ is the divergence, for axisymmetric flow

$$\tilde{D} \equiv \nabla \cdot \mathbf{V} \equiv \frac{1}{r}\frac{\partial (ru)}{\partial r} + \frac{\partial v}{\partial y}. \tag{6}$$

Since the cylinder with a disk is forced to oscillate sinusoidally along its longitudinal axis (see Fig. 1) as

$$y(t) = y(0) + a\sin(\omega t + \theta) \quad \text{for } t > 0, \tag{7}$$

the no-flux and no-slip velocity boundary conditions are imposed along the surfaces of the oscillatory cylinder and disks. The Neumann boundary condition for the pressure on the cylinder and disk surfaces is obtained by applying the momentum equations in the direction normal to the boundary. A symmetry boundary condition is prescribed on the axis of symmetry ($r = 0$). Because of very small amplitude and high frequency heave oscillation, disturbance of the free surface is expected to be small. This is consistent with experimental observations of Thiagarajan and Troesch (1998). Therefore, nonlinear free surface effects are not included in the present numerical modelling, instead a free-stream flow boundary condition is assumed, and pressure on the free surface is a constant. Free-stream velocity conditions are also applied to the entire open boundary. For the closure of the problem at the open boundary, approximate pressure conditions are employed at boundaries that are sufficiently far from the oscillating cylinder and disks.

2.2. Numerical procedures

The spatial derivatives in the governing equations, boundary conditions and grid equations are discretised with a finite difference method in the computational plane.

The discretisation of the convection terms of the momentum equations is of primary concern due to their nonlinear nature. This is particularly important for high Reynolds number flows since the convection is expected to be the dominant feature. In the present study, due to the very small KC numbers and high β, Reynolds number is expected to be moderate (laminar or transitional). A modified second-order four-point upwind scheme proposed by Kawamura and Kuwahara (1984) is used to discretise the nonlinear convection terms of the momentum equations,

$$\left(f\frac{\partial u}{\partial \xi}\right)_{i,j} = \frac{f_{i,j}}{12\Delta\xi}(-u_{i+2,j} + 8u_{i+1,j} - 8u_{i-1,j} + u_{i-2,j}) + \frac{|f_{i,j}|}{4\Delta\xi}(u_{i+2,j} - 4u_{i+1,j} + 6u_{i,j} - 4u_{i-1,j} + u_{i-2,j}). \tag{8}$$

Second-order central differencing is used for all the other terms,

$$\left(\frac{\partial f}{\partial \xi}\right)_{i,j} = \frac{f_{i+1,j} - f_{i-1,j}}{2}, \tag{9}$$

$$\left(\frac{\partial^2 f}{\partial \xi^2}\right)_{i,j} = f_{i+1,j} + f_{i-1,j} - 2f_{i,j}. \tag{10}$$

All the spatial terms in the transformed pressure Poisson equation are discretised by using second-order central differencing. However, those spatial derivatives in the boundary conditions are discretised by a second-order one-sided differencing, i.e. for the left boundary, we have,

$$\left(\frac{\partial f}{\partial \xi}\right)_{i,j} = \frac{-3f_{i,j} + 4f_{i+1,j} - f_{i+2,j}}{2}, \tag{11}$$

$$\left(\frac{\partial^2 f}{\partial \xi^2}\right)_{i,j} = f_{i+2,j} - 2f_{i+1,j} + f_{i,j}. \tag{12}$$

Similar spatial derivatives can be derived for all the other boundaries.

The method is to solve the nonlinear governing equations together with the given boundary conditions. A nonstaggered grid for the velocity and pressure is used in the present work. The primitive variables of velocity and pressure are obtained by solving momentum equations and pressure Poisson equation alternatively using an iterative method. In this study, the momentum Eqs. (3) and (4) are marched forward in time by using a second-order fully implicit scheme Beaudan and Moin (1994):

$$\frac{3\mathbf{V}^{n+1} - 4\mathbf{V}^n + \mathbf{V}^{n-1}}{2\Delta t} + \mathbf{V}^{n+1} \cdot \nabla \mathbf{V}^{n+1} = -\nabla p^n + \frac{1}{R'_e} \nabla^2 \mathbf{V}^{n+1}. \tag{13}$$

The discrete form of nonlinear (13) is first solved by using the Gauss–Seidel iterative method with pressure at time level (n). A solution for pressure at time level $(n+1)$ is then obtained by solving the discrete form of pressure Poisson equation (5) using successive over-relaxation (SOR) scheme. The correction term $(\partial \tilde{D}/\partial t)$ in the pressure Poisson equation is also discretised with the above second-order time-accurate scheme.

The theoretical formulation for the nonlinear initial boundary-value problem defined by the governing equations and boundary conditions was solved by using finite difference method based on curvilinear coordinates. The primitive variables, i.e. velocity and pressure were obtained by solving momentum equations and the Poisson equation alternately. Based on convergence tests, a mesh (134×150) with minimum mesh spacing of $\Delta x/R = 0.0005$ is constructed in such a way that the node points are concentrated near the cylinder and disk surfaces and stretched out gradually. The small regions around the sharp edges of the disks, where the vortices are generated and shed during the oscillations, are emphasised with clustering the grid points to the regions (see Fig. 2). All the calculations are carried out with a time step $\Delta t/T = 1/5000$. The mesh is regenerated at each time step according to the instantaneous position of the forced oscillation of the configuration. Fig. 3 shows the variation of damping ratio with the minimum grid spacing near the disk surface and the time step, respectively, for a cylinder with one or two disks attached. The numerical method has been extensively validated against benchmark problems and experimental measurements.

2.3. Calculation of force coefficients

The hydrodynamic heave force acting on the cylinder plus disks is calculated by integrating the vertical component of the stress vector along the structure surfaces,

$$F = -\int_B \left\{ -pn_y + \frac{1}{R_e}\left(\frac{\partial u}{\partial y} + \frac{\partial v}{\partial r}\right) n_r + \frac{2}{R_e}\frac{\partial v}{\partial y} n_y \right\} \mathrm{d}s, \tag{14}$$

where B denotes the surface area of the structure, p the dynamic pressure, and (n_r, n_y) the radial and axial components of the unit-normal vectors along the structure surface. The three terms of the right-hand side of the above expression represent the dynamic pressure component, the viscous shear-stress component and the normal viscous-stress component, respectively.

A Morison-like equation can be used to normalise the heave damping force of an oscillating cylinder cum disks

$$F_d(t) = \tfrac{1}{2}\varrho S C_d v(t)|v(t)|, \tag{15}$$

where $v(t)(= a\omega\cos(\omega t))$ is the velocity of oscillation. Since the cylinder and the disk are subjected to a sinusoidal oscillation, the drag and the added mass coefficients are obtained by Fourier analysis (Sarpkaya and Isaacson, 1981):

$$C_d = -\frac{3\omega}{4\varrho S U_m^2} \int_0^T F(t)\cos(\omega t)\,\mathrm{d}t, \tag{16}$$

$$C_a = \frac{1}{\pi \varrho \forall U_m} \int_0^T F(t)\sin(\omega t)\,\mathrm{d}t, \tag{17}$$

where $U_m(= a\omega)$ is the amplitude of the velocity of the oscillation, $\forall$ is displaced volume of the system, T and ω are the period and radial frequency of the oscillation.

An alternative expression of the drag force by using the equivalent linear damping coefficient B is

$$F_d(t) = Bv(t). \tag{18}$$

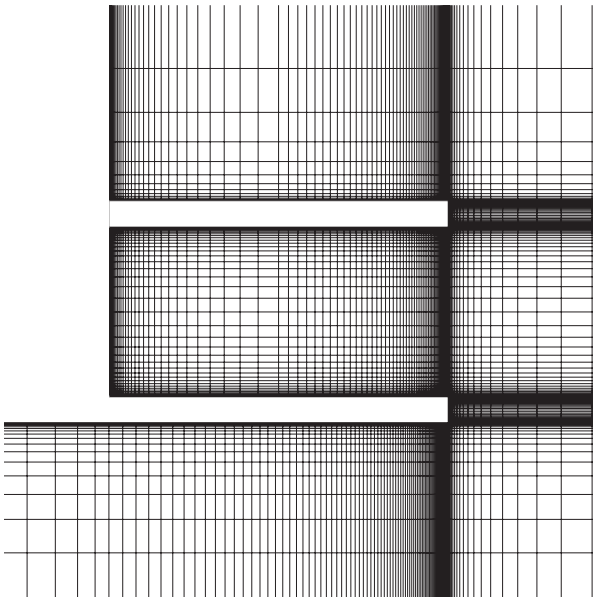

Fig. 2. Typical grid distribution around the surface of the cylinder and disks.

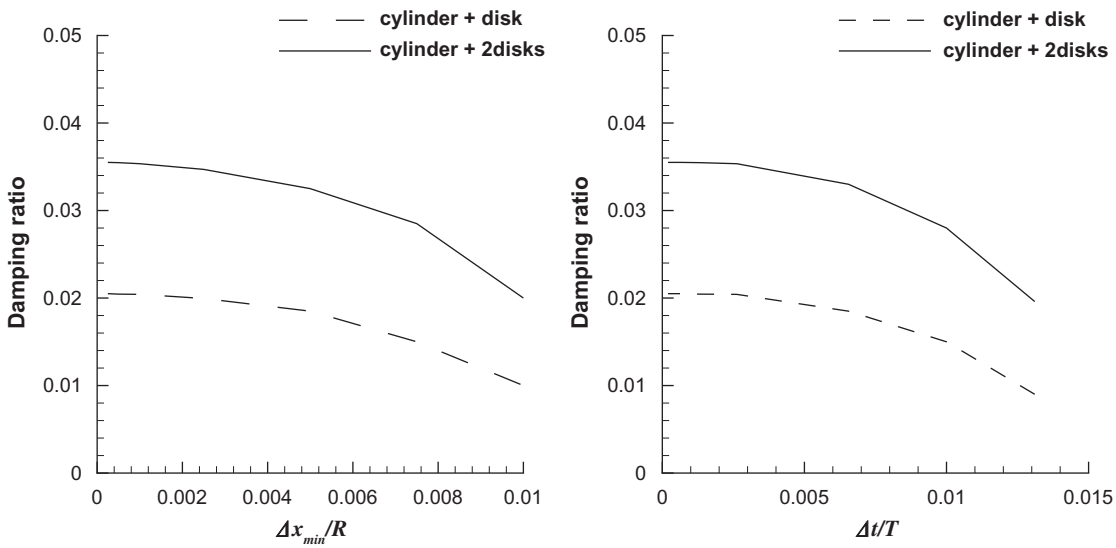

Fig. 3. Convergence tests.

By using Fourier-averaged approach, the equivalent linear damping coefficient is then obtained for a harmonic oscillation from Eqs. (15) and (18):

$$B = \tfrac{1}{3}\mu\beta D_d(\mathrm{KC})C_d, \tag{19}$$

where μ is the dynamic viscosity.

A nondimensional damping ratio may then be defined as

$$Z = \frac{B}{C}, \tag{20}$$

where $C = 2(m + m_a)\omega$, m and m_a represent the mass and added mass, respectively. In order to examine the dependence of the viscous damping on the geometry of the disk, the oscillating frequency is used in defining C instead of the natural

frequency of the system for the critical damping. Therefore, the damping ratio defined in Eq. (20) is a slightly modified damping ratio. By inserting expressions for the mass $m = C_m \varrho \forall$ and B, one can obtain the damping ratio

$$Z = \frac{1}{3\pi^2} C_G \frac{C_d}{C_m} \mathrm{KC}, \tag{21}$$

where C_G is a geometric constant

$$C_G = \frac{D_d^3}{(D_c^2 T_d + n D_d^2 t_d)} = \frac{1}{(D_c/D_d)^2 T_d/D_d + n(t_d/D_d)}, \tag{22}$$

where n is the number of disks. Eq. (22) shows that the constant C_G depends on the geometry of the configuration, and is a function of the number of disks, diameter ratio (D_c/D_d), aspect ratio (t_d/D_d) and draft diameter ratio (T_d/D_d) of the geometry.

3. Results and discussion

In addition to the convergence tests with varying flow domains and mesh parameters, the numerical procedures were also validated against two-dimensional benchmark problems: lid-driven flow in a square cavity and cross flow over a circular cylinder (Tao, 2002). In this paper, the present numerical method is further validated by comparing with the experimental results of Thiagarajan and Troesch (1998) for the flow of an oscillating truncated vertical cylinder with and without a circular disk attached at the keel. As can be seen in Fig. 4, the present numerical solutions agree well with the experimental results. Damping ratio of both numerical solutions and experimental measurements showed approximately linear trends in the range of KC = 0.1–1.0 and tends to be constant as KC → 0. The numerical results appeared to be in general larger than that suggested by the experimental data due to the difference of the edge sharpness of the cylinder bottom and/or disk in numerical modelling and experimental setup. Tao and Thiagarajan (2000) demonstrated that a very small radius of the edge can result in a significant reduction of the pressure drag.

Numerical simulations were conducted with a 198.1 m draft and 39.0 m diameter spar column, and a spar with one or two 0.475 m thick disks of 51.2 m diameter attached. Eight configurations comprising of the bare hull, spar with one disk or two disks of different span from 3.048 to 18.288 m, oscillating at different amplitudes at a constant period of 28 s were considered. The corresponding KC and β numbers were 0.112, 0.337, 0.561 and 7.869×10^7, respectively (see Table 1).

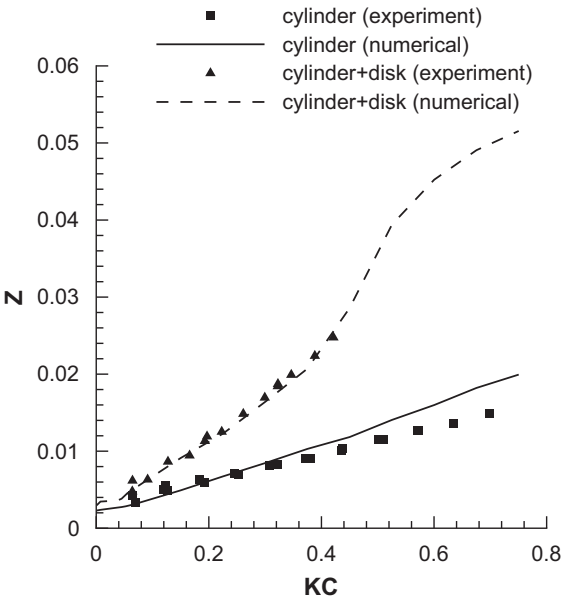

Fig. 4. Damping ratio Z versus KC for cylinder only and cylinder with a disk $(t_d/D_d = 0.0417)$ at $\beta = 89\,236$.

Table 1
Oscillation parameters and specifications of the configuration

Configuration	1	2	3	4	5	6	7	8
Spar diameter (m)				39.0				
Total draft (m)				198.1				
Disk thickness (m)	No disk	0.475	0.475	0.475	0.475	0.475	0.475	0.475
Disk diameter (m)	No disk	51.2	51.2	51.2	51.2	51.2	51.2	51.2
Diameter ratio (D_d/D_c)	No disk	1.31	1.31	1.31	1.31	1.31	1.31	1.31
Aspect ratio (t_d/D_d)	No disk	0.0093	0.0093	0.0093	0.0093	0.0093	0.0093	0.0093
Span (L)	No disk	0 (single disk)	3.048	6.096	9.144	12.192	15.24	18.288
Relative spacing (L/D_d)	No disk	0	0.078	0.156	0.234	0.313	0.391	0.469
Amplitude (m)		0.914		2.743			4.572	
KC		0.112		0.337			0.561	
Period (s)				28				
β				7.869×10^7				

3.1. Influence on flow structure

The present study presents flow visualisation for a circular cylinder column attached with two circular disks of different relative spacings to illustrate the mechanism underpinning the flow dynamics. The development of the vortex shedding pattern is shown by the vorticity plot in a meridional plane which is computed by taking the curl of the velocity field. In the axisymmetrical case

$$\zeta = \frac{\partial u}{\partial y} - \frac{\partial v}{\partial r}. \tag{23}$$

Fig. 5 shows the instantaneous distribution of vorticity at the same parameters $\beta = 7.869 \times 10^7$, $t_d/D_d = 9.286 \times 10^{-3}$, and $D_d/D_c = 1.313$ but different KC and relative spacing L/D_d. The figures of the three cases are equally spaced over one period starting at top dead centre (TDC). The solid and dashed lines represent positive and negative vorticity, respectively.

3.1.1. Effect of KC

First, we examine the influence of KC on the vortex shedding development by comparing Fig. 5(1a)–(1d) with Fig. 5(2a)–(2d). The two cases are of the same relative spacing of the disks ($L/D_d = 0.060$) at different KCs. The vortices generated by the sharp edges of the two disks were seen to travel around the disks' edges. In Fig. 5(1a)–(1d), the vortex shedding pattern is approximately symmetric about the mean position of the oscillation with strong interactions due to small relative spacing between the vortices of different edges at this particular value of KC = 0.112 and small relative spacing of the two disks. A vortex of positive vorticity shed from the top disk during upstroke is seen to be blocked by the ascending bottom disk and moving back to the bottom edge of the top disk. This vortex, reduced its strength due to partly amalgamation with the newly generated vortex of positive vorticity and travelling downwards, then convects away around the edges of the top disk during the next downstroke. However, the vortex ring of negative vorticity from the bottom disk during downstroke is unable to travel into the space between the two disks, instead convects away from the disk. Only a small vortex of negative vorticity shed from the upper edge of the bottom disk is able to reach the top disk and amalgamate with the major vortex ring convecting away from the disk.

When KC increases, as shown in Fig. 5(2a)–(2d) at KC = 0.337, the scale and strength of the vortices generated by the oscillating disks also increase resulting in stronger interaction of the two vortex shedding processes. In addition to the vortex shedding interaction which occurred within the space between the two disks, the major vortex rings of positive/negative vorticity induced by one disk are able to reach the edge of the other disk and interact directly with the vortex of the same positive/negative vorticity shed from the other disk. The asymmetric vortex shedding pattern shows the impact of the presence of the cylinder wall above the top disk to the vortex shedding development.

3.1.2. Effect of L/D_d

In order to illustrate the spacing effect of the heave plates on the vortex shedding process and viscous damping, vorticity of cylinder plus 2 disks of the same KC to Fig. 5(1a)–(1d) (KC = 0.112) and different L/D_d is calculated and plotted in Fig. 5(3a)–(3d).

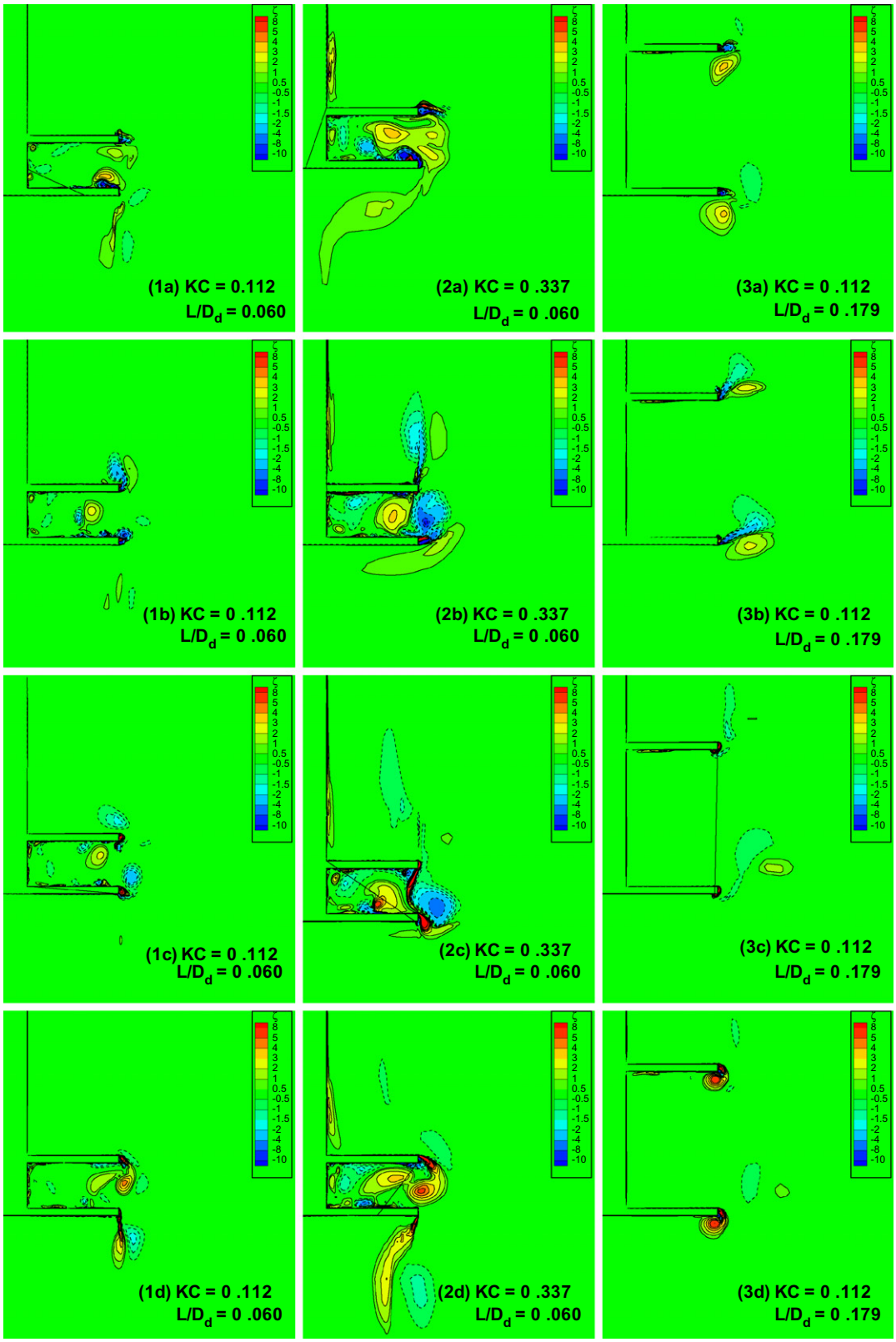

Fig. 5. Flow structure around the disk edges (dashed lines indicate negative vorticity).

Tao and Thiagarajan (2003a) demonstrated that three vortex shedding modes i.e. independent, interactive and asymmetric unidirectional vortex shedding, exist for the flow induced by oscillatory vertical cylinder with a disk attached at its keel. The occurrence of these modes were shown to primarily depend on KC and disk thickness-diameter ratio t_d/D_d. According to Tao and Thiagarajan (2003a), disk flow undergoes unidirectional vortex shedding as the condition: $(t_d/D_d)/\mathrm{KC}^{0.75} < 0.065$ is satisfied. For the present cases shown in Fig. 5(1a)–(1d) and Fig. 5(3a)–(3d), $\mathrm{KC} = 0.112$ and $t_d/D_d = 9.286 \times 10^{-3}$, this gives $(t_d/D_d)/\mathrm{KC}^{0.75} = 0.048$. For a large relative spacing case, two separated processes of the unidirectional vortex shedding of the two disks are clearly shown in Fig. 5(3a)–(3d). However, an interactive vortex shedding pattern is observed in the small L/D_d case (Fig. 5(1a)–(1d)) at the same KC and aspect ratio. This is a clear indication that the relative spacing not only affects vortex shedding development in the way that vortices developed within the two disks are suppressed, but also in the way that it changes the vortex shedding regime due to the strong interaction between the vortex shedding processes induced by the two disks.

It is observed that in Fig. 5(3a)–(3d), the shedding angles of the two vortex shedding processes due to the two disks are slightly different indicating that the flow does 'feel' the presence of the cylinder wall at the current values of KC and diameter ratio (D_d/D_c).

Graham (1980) revealed that for a 2-D plate with two edges normal to an oscillatory flow of small KC number, one edge tends to shed a vortex in one axial direction and the other edge in the opposite one leading to 'diagonal shedding' or 'antisymmetric' about the two edges. Tao and Thiagarajan (2003a) further demonstrated that, in the case of a thin circular disk with two edges the shedding at low KC tends to be constrained to be an axisymmetric and hence the diagonal mode is not possible. Further, the tendency to an asymmetric wake may also be reinforced in this case by the natural instability between a pair of counter-rotating coaxial vortex rings which tend to 'leapfrog' each other. The direction of such asymmetric unidirectional vortex shedding depends on the initial flow start-up conditions or later disturbances.

Fig. 6(a)–(h) shows instantaneous vorticity contours around the edges of the two disks calculated at $\mathrm{KC} = 0.337$ and $L/D_d = 0.179$ equally spaced intervals ($\frac{1}{8}T$) over one cycle. One distinct vortex shedding pattern is observed in flow visualisation. In contrast to the flow shown in Fig. 5(3a)–(3d) in which the two vortex pairs of the two disks shed along the same direction above the plane of the disks, the two vortex pairs in Fig. 6(a)–(h) appear to shed along opposite directions alternately at a large angle above and below the planes of the disks, respectively, resulting in 'alternate unidirectional vortex shedding'. Such an antisymmetric vortex shedding pattern occurs from the two disks oscillating along their axis because of the strong interaction between the two vortex shedding processes forcing one of the vortex shedding processes to change its direction. However, such an interaction is not strong enough to change the unidirectional vortex shedding pattern completely as shown in Fig. 5(1a)–(1d) and Fig. 5(2a)–(2d) due to smaller spacing of the disks. This demonstrates that the relative spacing of the disks has a significant effect on vortex shedding patterns of the two disks, and such an effect is dependent strongly on KC number.

The above two vortex shedding patterns are also observed for smaller spacing and lower KC at which very little influence of the cylinder wall to the two vortex shedding processes is observed as the scale and the travelling distance of the vortices are relatively small. This is a clear indication that the two vortex shedding patterns observed here are a bistable process as it would be if the cylinder was infinite and not truncated. However, the cylinder wall is expected to affect the vortex shedding process as the difference of the diameters of the disk and the cylinder is small and/or at an increasing KC number.

3.2. Influence on added mass

The added mass of an isolated circular disk oscillating along its axis equals to the mass of an ellipsoid of semi-axes a, b, c ($a = D_d/\pi$ and $b = c = D_d/2$, respectively) of water enclosing the disk (Sarpkaya and Isaacson, 1981),

$$m_a = \frac{4\pi}{3}\rho abc = \frac{1}{3}\rho D_d^3. \tag{24}$$

For a configuration of a cylinder with a disk attached to its base, if the diameter of the disk is greater than that of the cylinder, there is only a part of the disk on the cylinder side producing added mass effect due to the presence of the cylinder. If we assume that the entrained fluid moves as an attached homogeneous mass, by neglecting the interference between the cylinder and disk, the added mass of a cylinder plus disk may be written as

$$m_{1a} = \tfrac{1}{12}\rho(2D_d^3 + 3\pi D_d^2 z - \pi^3 z^3 - 3\pi D_c^2 z), \tag{25}$$

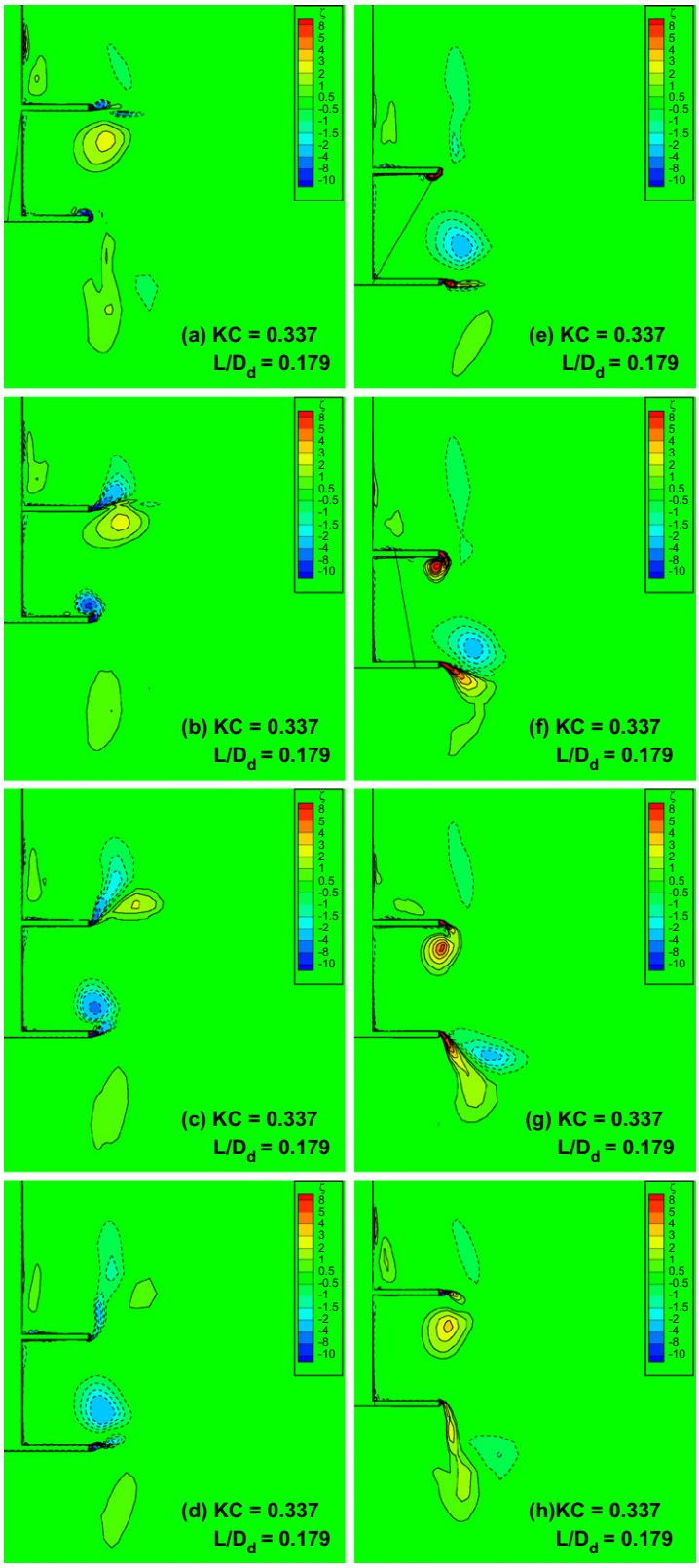

Fig. 6. Alternate unidirectional vortex shedding (KC = 0.337, $L/D_d = 0.179$).

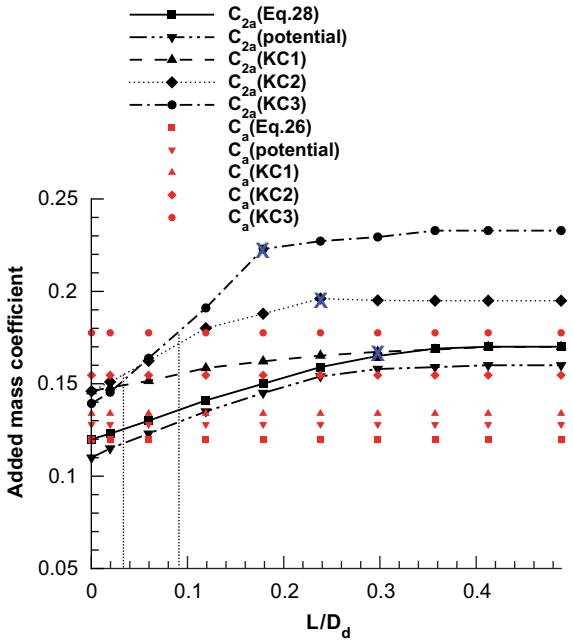

Fig. 7. Added mass coefficient as a function of relative spacing L/D_d.

where $z = \frac{1}{\pi}\sqrt{D_d^2 - D_c^2}$. The added mass coefficient, C_{1a}, of a cylinder plus disk is then obtained as the ratio of the added mass to the displaced mass $(m + m_a)$

$$C_{1a} = \frac{1}{3}\frac{2D_d^3 + 3\pi D_d^2 z - \pi^3 z^3 - 3\pi D_c^2 z}{\pi(D_d^2 t_d + D_c^2 T_d)}. \tag{26}$$

For a configuration of a cylinder with two disks attached, under the similar assumption that the entrained fluid between the two disks moves as an attached homogeneous mass, by neglecting the interference of the cylinder and disks, the added mass of cylinder plus 2 disks can be written as

$$m_{2a} = \tfrac{1}{48}\rho(8D_d^3 - 12\pi D_c^2 z - 12\pi D_c^2 L + 12\pi D_d^2 z - 4\pi^3 z^3 + 12\pi D_d^2 L - \pi^3 L^3). \tag{27}$$

The added mass coefficient, C_{2a}, of a cylinder plus 2 disks is then obtained as the ratio of the added mass to the displaced mass $(m + m_{2a})$,

$$C_{2a} = \frac{1}{12}\frac{(8D_d^3 - 12\pi D_c^2 z - 12\pi D_c^2 L + 12\pi D_d^2 z - 4\pi^3 z^3 + 12\pi D_d^2 L - \pi^3 L^3)}{\pi(2D_d^2 t_d + D_c^2 T_d)}. \tag{28}$$

As can be seen from Eqs. (25)–(28), the above approach also assumes that the added mass is independent of the amplitude of oscillation. In order to examine the influence of the relative spacing of the disks and KC, and further viscous effects on added mass, the added mass coefficients of a prototype spar hull with one and two disks attached in different spacing are calculated using the numerical method described in Sections 2.2 and 2.3 at different KC numbers.

Fig. 7 shows the added mass coefficient as a function of the relative spacing L/D_d at different KC. Also plotted in the figure is the added mass for the spar hull with one disk attached at its bottom. It is seen that a similar trend of the increasing added mass coefficient due to the increasing relative spacing for all three KC numbers is evident. In general, the additional disk indeed results in higher added mass coefficient at all three KC numbers. However, as can be seen in Fig. 7, at certain L/D_d values depending on KC, the added mass coefficients approach their asymptotic values. As shown in Eq. (28), when the spacing of the two disks reaches $2z$ (i.e. $L = 2z$), there will be no further increase of the added mass as L continue to increase. It is also seen in Fig. 7 that, if the spacing between the two disks is very small,

e.g. $L/D_d \leqslant 0.090$ for KC = 0.561 and $L/D_d \leqslant 0.0337$ for KC = 0.34 the added mass coefficients for the two-disks' cases are clearly smaller than the single-disk cases, respectively. For a configuration of a spar with two disks attached at a very small relative spacing, the water entrapped between the two disks oscillates with the system. Therefore, the two disks and the entrapped water physically oscillate as one disk of larger thickness. However, distinct differences of the added mass coefficients between the present numerical results of viscous flow and the value calculated by Eq. (28) is observed in Fig. 7. This is a clear demonstration that the effect of the entrained fluid between the two disks on the added mass for the configuration investigated is much more subtle and in fact is governed by local flow effects induced by factors such as flow separation and vortex shedding.

Also plotted in Fig. 7 are the potential flow solutions of the added mass coefficients for the two configurations. It is seen in Fig. 7 that the simplified formulas of Eqs. (26) and (28) slightly overestimate the added mass due to assumptions of homogeneous trapped fluid mass between the disks and neglecting the interference between the cylinder and disks. Such effects, as can be seen in Fig. 7, are more pronounced as the spacing between the two disks decreases. Fig. 7 also showed a significant influence of KC number on added mass due to viscous effects, and the added mass coefficient of the present numerical results calculated for viscous flow approaches the value of potential flow at very low KC. Fig. 8

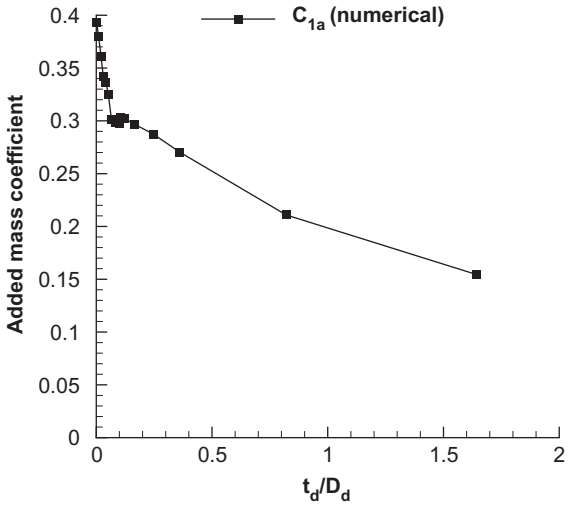

Fig. 8. Influence of disk thickness on added mass coefficient for cylinder plus disk configuration at KC = 0.75.

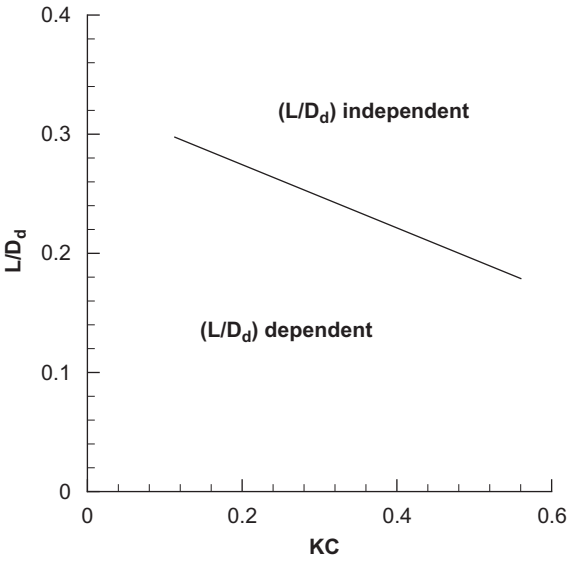

Fig. 9. Two added mass coefficient regions in terms of relative spacing L/D_d and KC.

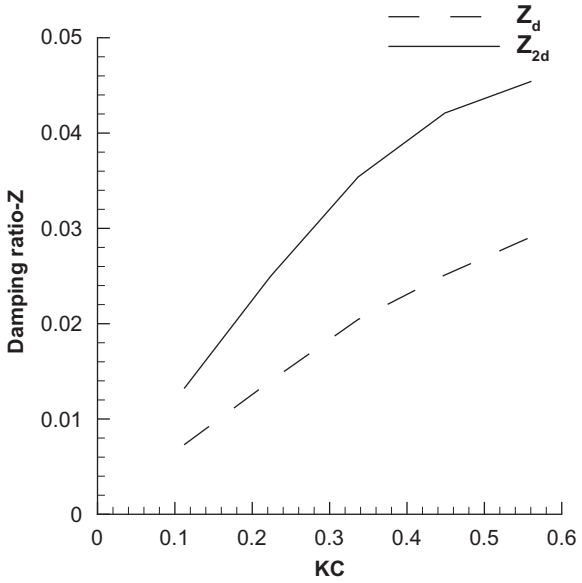

Fig. 10. Damping ratio for cylinder plus disk (Z_d) and cylinder plus 2 disks (Z_{2d}) as a function of KC for relative spacing $L/D_d = 0.357$.

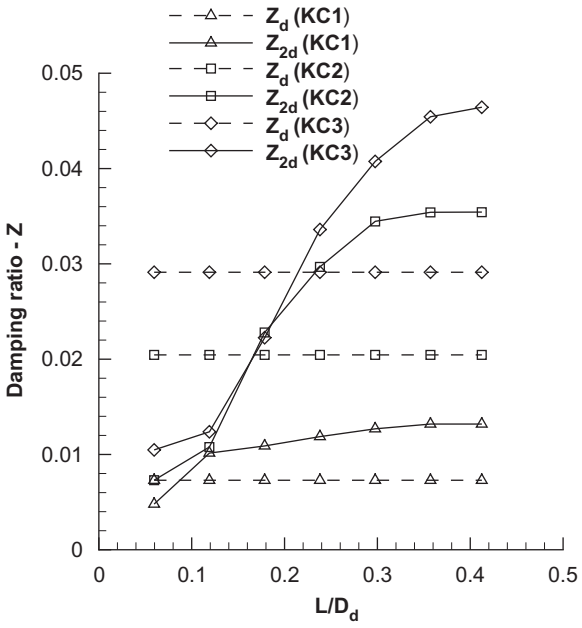

Fig. 11. Damping ratio as a function of relative spacing L/D_d.

demonstrates that for an axially oscillating cylinder with a disk attached at its keel, an increasing added mass coefficient evidently results from a thinner disk due to viscous effect.

Based on the characteristics of added mass coefficient of the configuration of a cylinder plus 2 disks shown in Fig. 7, by identifying the transitional points of the added mass coefficient at different KC numbers, we obtained the following chart (Fig. 9) representing the two regions in which the added mass coefficient is independent or dependent of the relative spacing of the disks, respectively. For a spar platform of a typical heave natural period 25–30 s, increasing added mass coefficient will result in increasing the heave natural period further outside the prevailing wave period

range. From the point of view of improving offshore structure operation safety by reducing undesired vertical oscillations of the spar, the disks should be arranged in the independent region in order to achieve maximum benefit.

3.3. Influence on hydrodynamic damping

In the present numerical simulation, it was observed that the vortex shedding effects are subject to starting transients which persist over approximately three periods of oscillation. After the initial three periods, a rather stable vortex shedding pattern was seen established. Such a transient effect is also evident in the force calculation—the damping ratio appears to be closely repeatable after the initial three periods of oscillation. Therefore, all the results of hydrodynamic damping presented in this paper are averages taken over period 6–10.

The viscous damping ratio was calculated for different KC numbers, and the dependence of the damping ratio (Z) on KC for a cylinder with one and two circular disks attached for a relative spacing $L/D_d = 0.357$ is plotted in Fig. 10. As can be seen in Fig. 10, approximately linear variation of damping ratio against KC is found for both cases. The reduced slope for a cylinder with two disks attached at high KC shown in the figure is primarily due to the more intensive interaction of the vortex shedding processes of the two disks as KC increases.

The dependence of the damping ratio (Z) on the relative spacing (L/D_d) for a cylinder with two circular disks attached oscillating at different KC numbers is plotted in Fig. 11. A general trend of increasing damping ratio as relative spacing increases is clearly observed in the figure. Compared to the single disk cases, damping ratios for all three cases of two disks (at different KC numbers) are smaller than their single disk counterparts at small spacing and greater than those at larger spacing. The crossing points represent the equal values of damping ratio for both the single disk and two-disks' cases at the same KCs. It is also observed that in flow visualisation, at a given KC, as the relative spacing of the two disks is very small, the water trapped between the two disks oscillates with the system. Therefore, the two disks and the trapped water physically oscillate as one disk of a larger thickness. The process of the vortex generation and shedding between the two disks are then suppressed to a large extent resulting in lower damping.

Fig. 12 shows a trend of increasing damping ratio with reducing aspect ratio (t_d/D_d) of the disk. The dependence of the viscous damping on the aspect ratio of the disk is more pronounced when the thickness is small. The reverse trend of increasing viscous damping for the thinner disk seen in Fig. 12 may be due to the forces of viscosity and convection cancelling each other in the small range of t_d/D_d from 0.11 to 0.17 at KC = 0.75. This is further demonstrated by the similar reverse trend of damping ratio occurring at different aspect ratios for cases of the same KC but different β (therefore Re), and different KC and the same β value shown in Fig. 12. As pointed out by Tao and Thiagarajan (2003b), the effects of geometry of the attached disk including t_d/D_d and D_d/D_c, are only important with combined effect of KC. Tao and Thiagarajan (2003a, b) further demonstrated that there exist three viscous damping regimes associated with the three vortex shedding modes due to an oscillating cylinder attached with a single disk of different thickness.

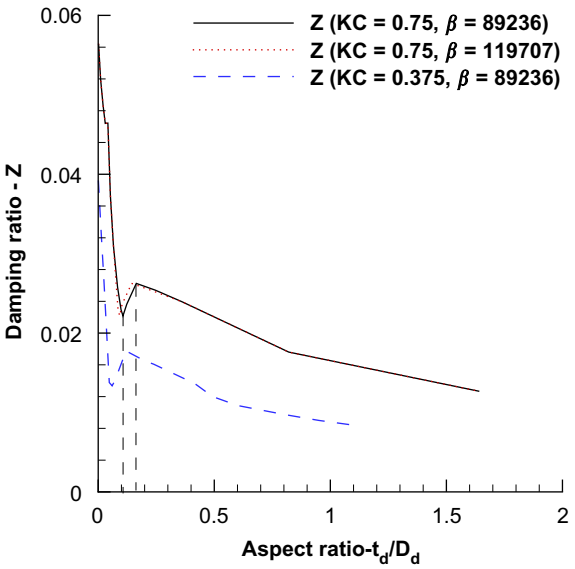

Fig. 12. Effect of disk thickness on viscous damping for cylinder plus disk at KC = 0.75.

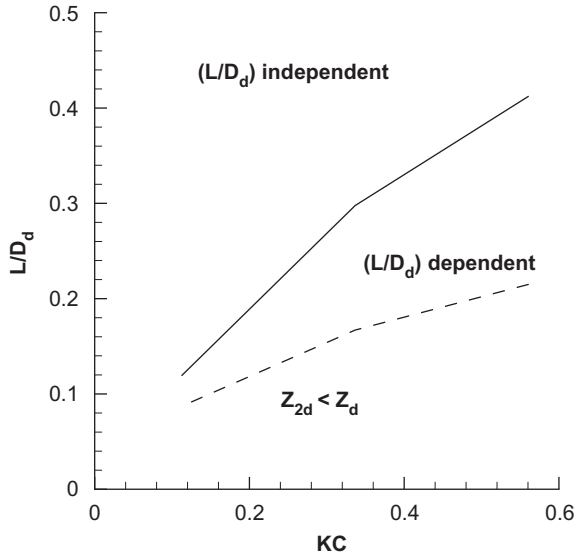

Fig. 13. Two damping regions in terms of relative spacing L/D_d and KC.

Also shown in Fig. 11 is that the damping ratios for all three cases of two disks increase rapidly at small relative spacing and approach their asymptotic values, respectively, as L/D_d continue to increase. The transitional points from which the damping appears to be independent of relative spacing are seen to be strongly dependent on the KC number. Similar to the approach applied to the added mass, by identifying the transitional points at different KC, we obtain the following chart representing the two damping regions in which the viscous damping of cylinder plus 2 disks configuration is independent and dependent of the relative spacing of the disks.

Fig. 13 shows that a L/D_d~KC chart is divided into three regions according to their viscous damping characteristics. In the region below the solid curve, the heave damping is dependent of the relative spacing, and a larger relative spacing results in higher damping of the configuration. While in the region above the solid line, damping becomes independent of L/D_d. The additional dashed curve shown in Fig. 13 represents the values at which the two configurations provide the same viscous damping. Therefore, below the dashed curve, the configuration of cylinder plus 2 disks produce lower damping than a cylinder plus disk due to the vortex shedding process between the two disks being suppressed at very small relative spacing.

Thiagarajan et al. (2002) reported that no appreciable change of damping from the configuration of spar plus 2 disks compared to spar plus disk in their experimental study. The relative spacing in the model test is $L/D_d = 0.2$ and $\mathrm{KC} = 0.13, 0.38, 0.64$. Applying these parameters to Fig. 13 yields very close damping values for both cases of the cylinder plus 2 disks and cylinder plus disk although the diameter ratio in the model test is slightly higher than that of Fig. 13.

From an engineering point of view, for the undesired motion of an offshore structure to be reduced via increasing hydrodynamic damping of the system, it is essential that the disks be arranged in the independent region to achieve maximum damping considering the typical KC range of the offshore structure. However, within the independent region, increasing L/D_d further will not bring much benefit in terms of viscous damping. It is noted that, however, in offshore system design, the location of the heave plates on the structure such as a spar/truss spar, is also subject to other considerations. These include, for example, the wave exciting force of the plate as a function of submergence. For some deep-water offshore structures such as a TLP, increased added mass may also tend to amplify the vertical oscillation due to increased heave natural period closer to the dominant wave energy range.

4. Conclusions

The following conclusions are drawn from this study.

1. The relative spacing of the disks is found to have the most striking effect on vortex shedding patterns induced by an oscillating cylinder with two thin disks attached. However, such an effect is dependent strongly on KC number.

Reducing relative spacing of the disks and/or increasing KC can result in 'alternate unidirectional vortex shedding' due to strong interaction between the two vortex shedding processes of the disks. It is further demonstrated that the relative spacing not only affects vortex shedding development in the way that the vortices developed within the two disks are suppressed, but also changes the vortex shedding regime due to the stronger interaction between the vortex shedding processes of the two disks as L/D_d continues to decrease.

2. Depending on KC, the additional disk is found to increase added mass as relative spacing of the disks increases. Two regions are found to exist within which the added mass coefficient shows independence or dependence on the relative spacing, respectively. In engineering design practice, it is recommended that the disks should be arranged in the independent region in order to achieve maximum benefit of reducing vertical oscillations due to increased heave natural period resulted from the increased added mass.
3. It is found that the heave plates configuration with a critical spacing depending on KC would be mostly beneficial in terms of maximizing damping of the system. Beyond that critical spacing, the heave damping appears to be independent of the spacing. Two regions of different characteristics of the heave damping are separated by the critical spacing depending on KC. The disks should be arranged in the independent region in order to achieve maximum benefit of motion suppression due to increased heave damping.
4. At very small relative spacing, the configuration of cylinder plus 2 disks is found to produce lower damping and added mass than a cylinder cum disk due to the vortex shedding process between the two disks being suppressed at very small relative spacing.
5. The charts representing relative spacing dependent and independent regions of added mass and damping are based on the results calculated under the current configuration such as aspect ratio (t_d/D_d) and diameter ratio (D_d/D_c) of the disks. For a different geometry of the configuration, Figs. 9 and 13 are subject to change.

Acknowledgements

The first author would like to thank Prof. J.M.R. Graham at the Department of Aeronautics, Imperial College of Science, Technology and Medicine and Dr Subrata Chakrabarti of Offshore Structure Analysis Inc., Chicago for their valuable discussions. The first author would also like to thank the support of the Griffith University Research Development Grant.

References

Beaudan, P., Moin, P., 1994. Numerical experiments on the flow past a circular cylinder at sub-critical Reynolds number. Report No. TF-62, Department of Mechanical Engineering, Stanford University, USA.

Cermelli, C.A., Roddier, D.G., 2005. Experimental and numerical investigation of the stabilising effects of a water-entrapment plate on a deepwater minimal floating platform. In: Proceedings of 24th International Conference on Offshore Mechanics and Arctic Engineering. Paper No. 67077.

Cozijn, J.L., Uittenbogaard, R., ter Brake, E., 2005. Viscous heave, roll and pitch damping of a deepwater CALM buoy with a skirt. In: Proceedings of 15th International Offshore and Polar Engineering Conference. Paper No. jsc-409, pp. 388–395.

Downie, M.J., Graham, J.M.R., Hall, C., Incecik, A., Nygaard, I., 2000. An experimental investigation of motion control devices for truss spars. Marine Structures 13, 75–90.

Graham, J.M.R., 1980. The forces on sharp-edged cylinders in oscillatory flow at low Keulegan–Carpenter numbers. Journal of Fluid Mechanics 97, 331–346.

Kawamura, T., Kuwahara, K., 1984. Computation of high Reynolds number flow around a circular cylinder with surface roughness. AIAA Paper No. 84-0340.

Lake, M., He, H., Troesch, A.W., Perlin, M., Thiagarajan, K.P., 2000. Hydrodynamic coefficient estimation for TLP and Spar structures. Journal of Offshore Mechanics and Arctic Engineering 122, 118–124.

Magee, A., Sablok, A., Maher, J., Halkyard, J., Finn, L., Datta, I., 2000. Heave plate effectiveness in the performance of truss spars. In: Proceedings of International Conference on Offshore Mechanics and Arctic Engineering, Paper No. OMAE2000/OSU OFT-4230.

Molin, B., 2001. On the added mass and damping of periodic arrays of fully or partially porous disks. Journal of Fluids and Structures 15, 275–290.

Prislin, I., Blevins, R.D., Halkyard, J.E., 1998. Viscous damping and added mass of solid square plates. In: Proceedings of 17th International Conference on Offshore Mechanics and Arctic Engineering.

Sarpkaya, T., Isaacson, M., 1981. Mechanics of Wave Forces on Offshore Structures. Van Nostrand Reinhold, New York.

Srinivasan, N., Chakrabarti, S.K., Radha, R., 2005. Damping-controlled response of a truss-pontoon semi-submersible with heave plates. In: Proceedings of 24th International Conference on Offshore Mechanics and Arctic Engineering. Paper No. 67522.

Tao, L., 2002. Numerical investigation of hydrodynamic heave damping of deep-water offshore structures. Ph.D. Thesis, The University of Western Australia.

Tao, L., Thiagarajan, K., 2000. The influence of edge sharpness on the heave damping forces experienced by a TLP column. In: Proceedings of 10th International Offshore and Polar Engineering Conference, vol. 1, pp. 277–282.

Tao, L., Thiagarajan, K., 2003a. Low KC flow regimes of oscillating sharp edges, I: vortex shedding observation. Applied Ocean Research 25 (1), 21–35.

Tao, L., Thiagarajan, K., 2003b. Low KC flow regimes of oscillating sharp edges, II: hydrodynamic force coefficients. Applied Ocean Research 25 (2), 53–62.

Thiagarajan, K., Troesch, A., 1998. Effects of appendages and small currents on the hydrodynamic heave damping of TLP columns. Journal on Offshore Mechanics and Arctic Engineering 120 (1), 37–42.

Thiagarajan, K., Datta, I., Ran, Z., Tao, L., Halkyard, J., 2002. Influence of heave plate geometry on the heave response of classic spars. In: Proceedings of International Conference on Offshore Mechanics and Arctic Engineering. Paper No. OMAE2002/OFT-28350.